Experimental analysis of double-diffusive and diffusive-layer-convection onset times and mixing velocities scalings

D. M. Escala [1,*] I. Castaldi [2] and A. De Wit [1,†]

[1] *Nonlinear Physical Chemistry Unit, Université libre de Bruxelles (ULB), CP231, Boulevard du Triomphe, 1050 Brussels, Belgium*

[2] *Aix-Marseille Université, CNRS, IUSTI, Marseille, France*

(Received 30 March 2026; accepted 20 July 2026; published 11 August 2026)

Statically stable stratifications of a less dense solution above a denser one can be destabilized in the gravity field when differential diffusion effects come into play. Specifically, if the stratification involves two solutes that diffuse at different rates, nonmonotonic density profiles can build up. Local convective zones develop then in the areas where, locally, the density decreases along the gravity field. Previous theoretical works have shown that for both double-diffusive (DD) and diffusive-layer-convection (DLC) regimes, the onset time and the mixing velocity of these buoyancy-driven instabilities are controlled by the dynamic density jump across these unstable zones. We provide here an experimental validation of these scalings by analysis of convective dynamics induced by differential diffusion around horizontal stratifications confined within a Hele-Shaw cell. We analyze a wide range of solute combinations and concentrations to vary the two important parameters of the problem which are the diffusion coefficients ratio δ and the buoyancy ratio R. By measuring the mixing length evolution, we quantify in each case the mixing velocity and the instability onset time. We show that, in both DD and DLC regimes, the convective dynamics are indeed governed by the dynamically generated local adverse density difference. In the DD case, the mixing velocity increases linearly with the dynamically induced density difference, while the onset time decreases accordingly. In the DLC regime, these properties are controlled by the local adverse density jump developing independently within each layer. The experimentally obtained scalings confirm the previous theoretical predictions and provide a quantitative framework for controlling buoyancy-driven mixing in stratified two-solute systems.

DOI: 10.1103/2d3q-f432

I. INTRODUCTION

Buoyancy-driven instabilities are genuinely observed in numerous flows in nature and engineering [1]. When two initially stratified miscible fluids are brought into contact in the gravity field, convective motions can develop in presence of density gradients and significantly enhance vertical transport and mixing [1–3]. Such buoyancy-induced mixing processes appear in a wide range of applications, including geological flows [4], oceanography [5], transport in porous media [2], reactive flows [6–11], carbon sequestration in saline aquifers [12–15], and dissolution processes [16]. In these systems, density gradients act as the driving force for convective instabilities that reshape the initially stratified configuration and govern the overall mixing dynamics.

When two different solutes contribute to the density of the fluid, a Rayleigh-Taylor (RT) instability develops when the upper solution is denser than the lower one. The RT dynamics can

*Contact author: dario.martin.escala@ulb.be

†Contact author: anne.de.wit@ulb.be

 ©2026 American Physical Society

be affected by differential diffusion effects giving rise, in some cases, to new mixed modes [17,18]. If, in contrast, the less dense solution is on top, the system is initially statically stable but, if the two species diffuse at different rates, diffusion alone can then destabilize the system [19–23]. If the solute in the denser lower layer diffuses faster than the solute in the less dense upper layer, a double-diffusive (DD) instability can develop, leading to a fingered deformation of the interface [1,10,22–28]. This mechanism is closely related to salt fingering in the ocean, where differential diffusion between heat and salt drives thermohaline convection [5,23,29]. In contrast, if the solute in the upper, less dense layer diffuses faster, a diffusive-layer-convection (DLC) instability may arise [10,20,22,30,31]. In this case, faster downward diffusion of the upper solute creates a depletion zone above the interface and an accumulation zone below it. As a result, locally unstable density stratifications form on either side of the initial contact line, generating convective rolls that initially develop independently in both layers [17,21,22].

Recent works have demonstrated, through combined experimental and numerical approaches for porous media flows, that differential diffusion effects can produce nonmonotonic density profiles characterized by dynamically evolving density jumps that differ from the one in the initial stratification [17,18,22]. The onset time and growth rate of buoyancy-driven fingers are governed by these dynamically generated density differences rather than by the initial density jump [18,32,33]. This framework has been extended to bulk flows governed by the Navier-Stokes equations, confirming that differential diffusion can significantly modulate both the onset and the intensity of convection through the formation of nonmonotonic density distributions [34,35]. These developments have been further extended by considering additional physical mechanisms. In particular, the influence of nonideal transport has been addressed, showing that concentration-dependent diffusivities can substantially modify the structure and evolution of double-diffusive instabilities [36]. Differential diffusion has also been explored in reactive systems, where extended classifications of buoyancy-driven instabilities have been proposed, identifying new regimes arising from the coupling between reaction kinetics and transport processes [7,10,13,37,38]. The interplay between imposed flow and differential diffusion has also been investigated in microfluidic configurations, highlighting its impact on mixing efficiency and pattern formation in continuous-flow systems [39]. Together, these results emphasize the increasing complexity of differential-diffusion-driven flows when additional physical mechanisms such as nonideal diffusion, chemical reactions, and imposed flows are taken into account.

In this context, theoretical scalings predicting the onset time of differential diffusion convective modes as well as their mixing velocity as a function of concentrations and diffusion coefficients of the solutes have been proposed for nonreactive systems [18,33]. First, it has been shown by combined modeling and experiments that differential diffusion affects the scalings of the Rayleigh-Taylor instability [18], when starting from a statically unstable case of a denser solution above a less dense solution. More recently, these scalings have been generalized theoretically to the DD and DLC cases [33], pertinent to the reverse initially stable case of a less dense solution above a denser one. But, these predictions have up to now not been tested experimentally, which hinders the validation of general scalings for buoyantly-driven instabilities around horizontal stratifications.

In this context, we fill this gap by providing an experimental validation of the theoretical scalings quantifying the buoyancy-driven DD and DLC instabilities induced by differential diffusion in initially stably stratified systems. To do so, we analyze experimentally the convective regimes developing around two-solute configurations confined in a quasi-two-dimensional reactor. For various combinations of solutes, we quantify the evolution of the mixing length L of the convective zone to determine the dependence of the mixing velocity $\tilde{U}$ and instability onset time $\tilde{\tau}_D$ on the locally generated adverse density difference produced by differential diffusion. Our experimental results confirm that the convective dynamics are governed by the dynamically induced density jump rather than by the initial density stratification as predicted by previous theoretical and numerical developments [33]. Our experimental validation of these scalings paves the way to control mixing induced by both DD and DLC hydrodynamic instabilities.

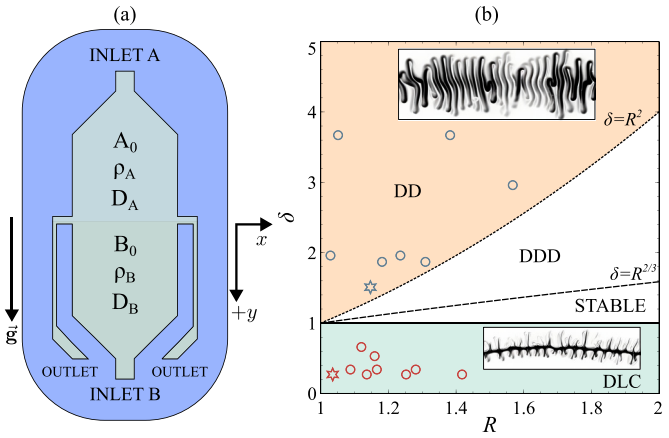

FIG. 1. (a) Schematic representation of the injection device used to conduct the experiments. The two aqueous solutions are injected simultaneously through the upper (solution A) and lower (solution B) inlets. They meet at the center of the Hele-Shaw cell and exit through the lateral outlets, creating a flat horizontal interface. The initial configuration is always statically stable, with the denser solution located in the lower layer. (b) Parameter space spanned by the buoyancy ratio R and the diffusivity ratio δ. All experiments correspond to initially stable stratifications ($R > 1$) and fall within the pure double-diffusive (DD) and pure diffusive-layer-convection (DLC) regimes. The solid line $\delta = 1$ separates DD ($\delta > 1$) from DLC ($\delta < 1$) configurations, while the dashed lines $\delta = R^2$ and $\delta = R^{2/3}$ indicate the boundaries of the delayed double-diffusive (DDD) and stable regions, respectively [22]. Insets show representative Schlieren images for each regime. The starred symbols correspond to the two reference cases shown in the insets, namely $(R, \delta) = (1.1469,\ 1.51)$ for DD and $(1.0354,\ 0.27)$ for DLC.

II. EXPERIMENTAL SETUP AND METHODS

Experiments were conducted in a vertically oriented Hele-Shaw (HS) cell composed of two transparent glass plates separated by a uniform gap width $h = 0.3$ mm. For this gap size, the characteristic length scales of the flow remain sufficiently large compared to the gap thickness, such that the dynamics can be described by Darcy's law [18,40,41]. Within the HS cell, two miscible, optically transparent aqueous solutions, denoted A (upper layer) and B (lower layer), with different initial compositions, concentrations, and densities, were brought into contact along a horizontal interface using a controlled injection protocol [42]. The experimental setup and injection procedure are schematically shown in Fig. 1(a).

All experiments were initialized in a hydrodynamically stable configuration, i.e., the less dense solution A was always placed above the denser solution B. Any subsequent destabilization of the interface is therefore induced solely by differential diffusion effects. Differential diffusion was achieved by preparing aqueous solutions containing combinations of four different solutes: sodium chloride (NaCl), potassium chloride (KCl), sucrose, and glycerol (all from Sigma-Aldrich). Stock solutions at a concentration of 1.2 M were prepared using reagent-grade chemicals and deionized water, without further purification. The working solutions were obtained by diluting and mixing these stock solutions to reach the desired initial concentrations and density difference.

The densities of pure water, $\tilde{\rho}_0$, and of the initial solutions A and B, $\tilde{\rho}_A$ and $\tilde{\rho}_B$, respectively, were measured using a DMA 35 Anton Paar density meter. From these measurements, we computed the dimensionless buoyancy ratio $R = \frac{\tilde{\rho}_B - \tilde{\rho}_0}{\tilde{\rho}_A - \tilde{\rho}_0}$ and the dimensional initial density difference $\Delta\tilde{\rho}_0 = \tilde{\rho}_A - \tilde{\rho}_B$. The ratio of diffusion coefficients, $\delta = \frac{D_B}{D_A}$, was obtained for each pair of solutes using tabulated diffusion coefficients reported in Table I. Although aqueous glycerol solutions may exhibit non-ideal density behavior at high concentrations, the solutions employed in this work (maximum concentration 1.2 M, corresponding to approximately 8.8 wt%) remain well within the

TABLE I. Diffusion coefficients D_i of the solutes used in experiments

Solute	D (10^{-5} cm^2/s)	Ref.
NaCl	1.54	[43]
KCl	1.91	[43]
Sucrose	0.52	[47]
Glycerol	1.02	[48]

range where tabulated density data show an essentially linear dependence on concentration [43]. Therefore, nonideal density effects are expected to be negligible under the present experimental conditions. All experiments were conducted within a controlled environment, where temperature was maintained at 22 °C and the density $\tilde{\rho}_0$ of pure water was measured to be 998.0 kg/m^3.

The various experimental cases studied in this work are summarized in the (R, δ) parameters space shown in Fig. 1(b). As can be seen, each (R, δ) combination corresponds to either the pure DD ($\delta > 1$, gray circles) or pure DLC ($\delta < 1$, red circles) regime. The two cases marked with a star correspond to the representative images of each regime shown as insets.

As the use of color indicators or dyes can modify the dynamics [44,45], the flows were visualized by tracking gradients of the refractive index of the aqueous solutions using a Schlieren technique, which provides a qualitative measurement of spatial density gradients within the HS cell [46].

The statistical analysis of the results was performed over six independent experiments for each value of the experimental parameters. Reported values correspond to the mean of the measurements, while error bars represent the associated standard deviation. Weighted least-squares regressions were performed using the inverse variance of each data point as statistical weights. For logarithmic representations, error bars were obtained by standard first-order propagation of the experimental errors. All reported uncertainties of the fitted parameters correspond to 95% confidence intervals (CI). The goodness of fit was quantified using the weighted coefficient of determination, R_0^2, for regressions constrained to pass through the origin, and the conventional weighted coefficient of determination, R^2, for all other regressions.

III. RESULTS

Let us first discuss general aspects of the two buoyancy-driven DD and DLC mechanisms investigated and the methodology used to characterize their dynamics. The system is initially prepared in a stable stratification, with the less dense solution A injected in the upper part of the Hele-Shaw cell and the denser solution B in the lower part. Upon contact, a flat interface is formed. As time progresses, this initially sharp interface broadens diffusively and eventually deforms due to convection driven by differential diffusion between the dissolved species. This leads to the emergence of fingered convective patterns characteristic of DD and DLC instabilities [17]. Representative snapshots of both regimes are shown in Fig. 2.

To quantify the mixing induced by these instabilities, we measure the mixing length L, defined as the vertical distance between the uppermost and lowermost positions reached by the fingers. A graphical illustration of L is provided in the last snapshot of the pure DD case in Fig. 2. The procedure used to extract L from the experimental images is detailed in Fig. 6 in the Appendix. The temporal evolution of L exhibits two distinct regimes [see Fig. 3(a)]. At early times, mixing is diffusion-dominated and L increases as $\sqrt{t}$. Once convection develops, L grows linearly with time. The transition between these regimes defines the onset time of convection, denoted $\tilde{\tau}_D$. The mixing velocity $\tilde{U}$ is obtained from the slope of a linear fit to $L(t)$ in the convective regime, i.e., $\tilde{U} = \Delta L/\Delta t$. Only the initial linear convective regime was used to determine the mixing velocity. Later stages of the evolution, where nonlinear interactions such as shielding and merging of fingers become significant, were excluded from the fitting procedure.

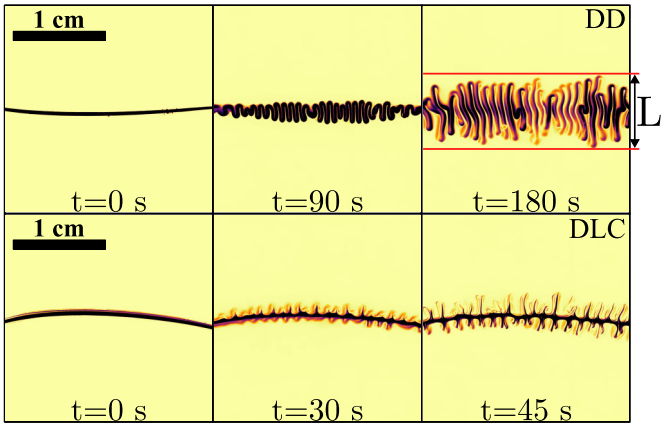

FIG. 2. Snapshots of two representative experiments illustrating the temporal development of the pure double-diffusive (DD, upper row) and pure diffusive-layer-convection (DLC, lower row) instabilities. The two experiments correspond to the cases marked with stars in Fig. 1(b). In the DD case, the instability develops across the interface, giving rise to fingerlike structures that grow symmetrically upward and downward. In contrast, in the DLC case, the instability leads to convective motions developing on either side of a stable central layer. In the last snapshot of the DD case, the two red horizontal lines define the mixing length L, measured as the vertical distance between the uppermost and lowermost points reached by the fingering structures. All images were processed and rescaled for visualization purposes (see Fig. 7 in the Appendix for details). The movies corresponding to these experiments are included as Supplemental Material [49].

Figures 3(b) and 3(c) present the temporal evolution of the averaged mixing length L for all solute combinations investigated in the pure DD and pure DLC regimes, respectively. Each curve corresponds to the mean mixing length obtained from six independent experimental realizations for a given (R, δ) combination, while the shaded regions represent the corresponding standard deviation.

Previous studies have shown that, for initially stable stratifications, the growth of fingers is not controlled by the initial density difference $\Delta\rho_0$, but rather by the locally generated adverse density difference $\Delta\rho_m$ induced by differential diffusion [18,33]. This dynamically generated density jump can be obtained from the base-state dimensionless density profile,

$$\rho(y,t) = A(y,t) + R\,B(y,t), \tag{1}$$

where $A(y,t)$ and $B(y,t)$ are the dimensionless diffusive concentration profiles in the absence of convection, given by

$$A(y,t) = \frac{1}{2}\mathrm{erfc}\left(\frac{y}{2\sqrt{t}}\right), \quad B(y,t) = \frac{1}{2}\mathrm{erfc}\left(-\frac{y}{2\sqrt{\delta t}}\right). \tag{2}$$

When the solutes diffuse at different rates ($\delta \neq 1$), the density profile can become nonmonotonic. In this case, a local maximum $\rho_{\max}$ and minimum $\rho_{\min}$ appear around the region where $\partial\rho/\partial y < 0$ [32]. The resulting dynamically induced density jump is defined in that region as $\Delta\rho_m = \rho_{\max} - \rho_{\min}$. An analytical expression for $\Delta\rho_m$, which depends only on R and δ and is independent of the governing flow equations and time, can be derived from Eqs. (1)–(2) as [33]:

$$\Delta\rho_m = \mathrm{erf}\left(\sqrt{\frac{\ln(\delta/R^2)}{2(1-1/\delta)}}\right) + R\,\mathrm{erf}\left(-\sqrt{\frac{\ln(\delta/R^2)}{2(\delta-1)}}\right). \tag{3}$$

This dimensionless density difference $\Delta\rho_m$ can be converted into a dimensional density jump $\Delta\tilde{\rho}_m$ as $\Delta\tilde{\rho}_m = \Delta\rho_m(\tilde{\rho}_A - \tilde{\rho}_0)$.

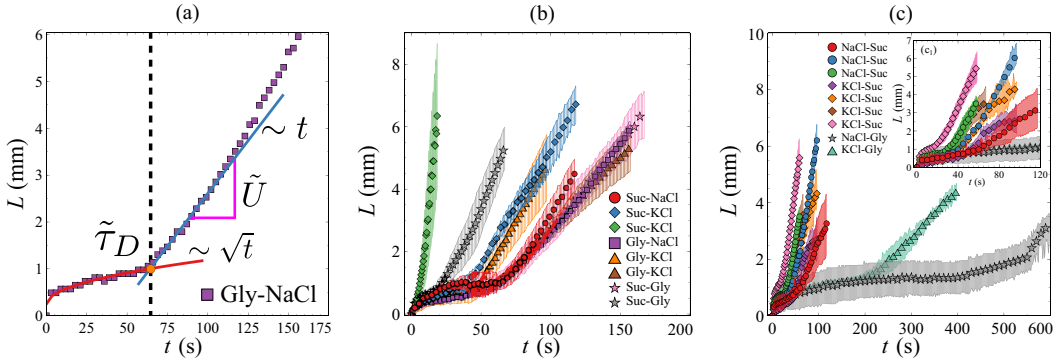

FIG. 3. (a) Temporal evolution of the mixing length L for the representative DD experiment $(R, \delta) = (1.1469,\ 1.51)$, illustrating the method used to compute the induction time $\tilde{\tau}_D$ and the mixing velocity $\tilde{U}$. After an initial diffusive regime characterized by $L \sim \sqrt{t}$, the system transitions to a convective regime in which L grows linearly with time. The dashed vertical line indicates the induction time $\tilde{\tau}_D$ obtained from the intersection of the diffusive and convective fits. $\tilde{U}$ is computed from the slope of the linear fitting of the convective regime. (b) Temporal evolution of L for all pure DD experiments. Each symbol and color correspond to a specific solute pair and set of initial conditions, as indicated in the inset. The shaded regions represent the standard deviation around the average mixing length obtained from six independent repetitions of the experiment. (c) Same as panel (b), but for all pure DLC experiments. Inset (c_1) shows a magnified view of the early-time evolution to facilitate comparison between the different experiments.

A. Pure DD regime ($1 \leqslant R^2 \leqslant \delta$)

In the DD regime, $\delta > 1$ as the solute B dissolved in the lower and denser layer diffuses faster than the solute A in the upper layer. As it diffuses upward, it locally increases the density of the upper solution. At the same time, solute depletion in the lower layer reduces the local density there. This differential diffusion effect can generate a nonmonotonic density profile and produce a local adverse density jump $\Delta\rho_m$ that drives the convective dynamics [see Fig. 4(a)].

All experimental values of parameters corresponding to the DD cases investigated here are summarized in Table II. As a representative example, we focus on the case $(R, \delta) = (1.1469, 1.51)$ (Expt. 4) for which a less dense solution of glycerol is put initially above a denser solution of

TABLE II. Combination of solutes used in the DD regime. Each symbol correspond to the experiments of Figs. 3(b), 4(b), and 4(c). For each case, the experimentally measured dimensional solution densities, initial concentrations, diffusion ratio δ, buoyancy ratio R, dimensional initial density jump $\Delta\tilde{\rho}_0$, and dynamic density jump $\Delta\tilde{\rho}_m$, are listed. In all cases, $\tilde{\rho}_0 = 998.0$ kg/m^3.

Expt.	Sym.	A	B	A_0 (M)	B_0 (M)	$\tilde{\rho}_A$ (kg/m^3)	$\tilde{\rho}_B$ (kg/m^3)	R	δ	$\Delta\tilde{\rho}_0$ (kg/m^3)	$\Delta\tilde{\rho}_m$ (kg/m^3)
1	●	Suc.	NaCl	0.20	1.00	1023.9	1038.6	1.5676	2.96	−14.7	0.6369
2	◆	Suc.	KCl	0.30	1.20	1038.0	1053.3	1.3825	3.67	−15.3	5.2998
3	◆	Suc.	KCl	0.40	1.20	1050.6	1053.3	1.0513	3.67	−2.7	14.6254
4	■	Gly.	NaCl	1.20	0.90	1030.0	1034.7	1.1469	1.51	−4.7	0.7015
5	▲	Gly.	KCl	1.20	0.80	1030.0	1035.8	1.1813	1.87	−5.8	1.7534
6	▲	Gly.	KCl	1.20	0.90	1030.0	1039.9	1.3094	1.87	−9.9	0.3079
7	★	Suc.	Gly.	0.20	1.20	1023.9	1030.0	1.2355	1.96	−6.1	1.1135
8	★	Suc.	Gly.	0.24	1.20	1029.1	1030.0	1.0289	1.96	−0.9	4.4891

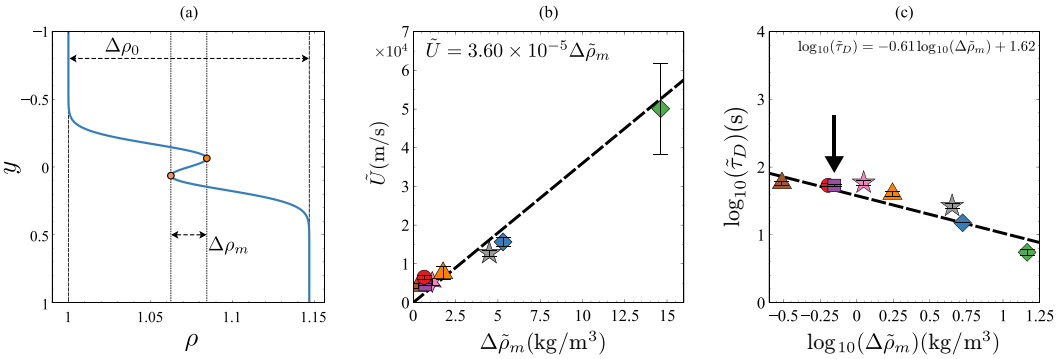

FIG. 4. Properties of the DD experiments. (a) Dimensionless diffusive base-state density profile $\rho(y) = A(y,t) + R\,B(y,t)$ computed using Eqs. (2), for $t = 0.05$ and $(R, \delta) = (1.1469,\ 1.51)$. Although the initial density difference $\Delta\rho_0 < 0$ corresponds to a statically stable stratification, differential diffusion induces a nonmonotonic density profile featuring a local adverse density difference $\Delta\rho_m$ that governs the instability dynamics. (b) Experimental average mixing velocity $\tilde{U}$ measured in the DD convective regimes as a function of the dynamic density difference $\Delta\tilde{\rho}_m$. The dashed line shows the weighted linear relation $\tilde{U} = 3.60 \times 10^{-5}\,\Delta\tilde{\rho}_m$. (c) Dependence of the experimental onset time $\tilde{\tau}_D$ on $\Delta\tilde{\rho}_m$. The dashed line corresponds to the regression $\log_{10}(\tilde{\tau}_D) = -0.61\ \log_{10}(\Delta\tilde{\rho}_m) + 1.62$. The arrow indicates the experimental case used to compute the base-state density profile shown in panel (a). Details of the statistical analysis of the fitted parameters are provided in the text. All data points share the same color code and symbols as in Fig. 3(b) and Table II.

NaCl. The associated base-state density profile is shown in Fig. 4(a). For this configuration, the dimensional initial density jump is $\Delta\tilde{\rho}_0 = \tilde{\rho}_A - \tilde{\rho}_B = -4.7$ kg/m^3, indicating a globally stable stratification as $\tilde{\rho}_A < \tilde{\rho}_B$. However, differential diffusion generates a local adverse density jump $\Delta\tilde{\rho}_m = 0.7015$ kg/m^3, which is positive and therefore destabilizing. This example illustrates how a system that is initially stable according to the global density jump ($\Delta\tilde{\rho}_0 < 0$) can become unstable due to the dynamically induced local unstable density difference ($\Delta\tilde{\rho}_m > 0$).

According to previous theoretical and numerical studies, once convection sets in because of the local $\Delta\tilde{\rho}_m > 0$, the mixing length L grows linearly in time and the corresponding mixing velocity $\tilde{U}$ scales with this dynamically generated adverse density difference $\Delta\tilde{\rho}_m$. In parallel, the onset time $\tilde{\tau}_D$ decreases as $\Delta\tilde{\rho}_m$ increases, since stronger local buoyancy forces induce an earlier transition from the diffusive to the convective regime [33].

The experimental results reported in Fig. 4(b) confirm these predictions. The measured mixing velocity $\tilde{U}$ increases linearly with $\Delta\tilde{\rho}_m$, following the weighted scaling $\tilde{U} = a\,\Delta\tilde{\rho}_m$, with a fitted coefficient $a = 3.60 \times 10^{-5}$ (95% CI: $[2.07 \times 10^{-5}, 5.13 \times 10^{-5}]$) and $\mathsf{R}_0^2 = 0.8160$.

The fitted slope agrees well with the theoretical prediction for buoyancy-driven flow in a Hele-Shaw cell, $\tilde{U} = \frac{gK}{\mu}\,\Delta\tilde{\rho}_m$, where $g = 9.81$ m/s^2 is the gravitational acceleration, $K = h^2/12$ the cell permeability with $h = 0.3$ mm, and μ the dynamic viscosity. Dynamic viscosities were estimated from tabulated literature data for the initial solutions at the experimental conditions [43,50,51]. The maximum estimated viscosities were approximately 1.07 mPa s for NaCl (1.2 M), 0.99 mPa s for KCl (1.2 M), 1.23 mPa s for glycerol (1.2 M), and 1.48 mPa s for sucrose (0.4 M), all remaining within approximately a factor of 1.5 of the viscosity of pure water. These values are those of the initial unmixed solutions and therefore provide an upper estimate of the viscosities involved during convective mixing. The good agreement between the experimental prefactor and the theoretical Darcy scaling further supports the interpretation that the mixing velocity is primarily controlled by the dynamically generated adverse density difference, which can be predicted analytically from R and δ through Eq. (3).

A consistent trend is also observed for the onset time, as shown in Fig. 4(c). The instability develops earlier as $\Delta\tilde{\rho}_m$ increases, and this dependence is well captured by the weighted best-fit

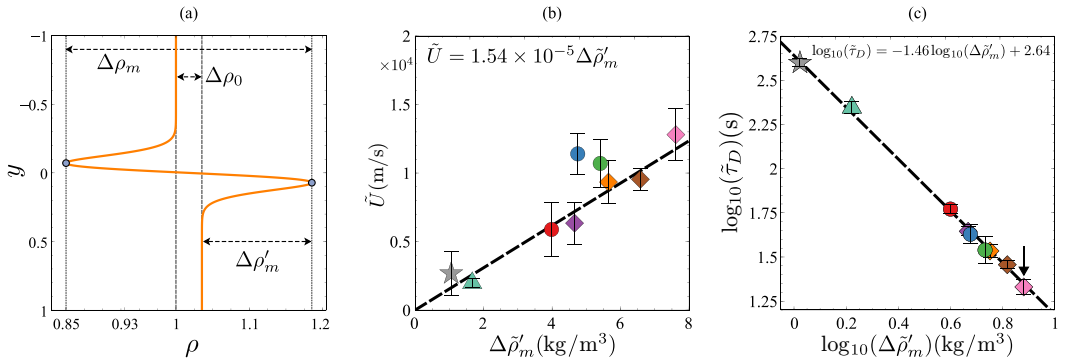

FIG. 5. Properties of the DLC experiments. (a) Diffusive base-state density profile $\rho(y) = A(y,t) + R\,B(y,t)$ computed using Eqs. (2) at $t = 0.05$ for $(R, \delta) = (1.0354,\ 0.27)$, corresponding to a pure diffusive-layer-convection (DLC) regime. Although the initial stratification is hydrodynamically stable, differential diffusion induces a nonmonotonic density profile featuring two locally unstable regions. In this case, the dynamics is governed by the local adverse density difference $\Delta\rho'_m$ rather than $\Delta\rho_m$. The initial bulk density difference $\Delta\rho_0$ is also indicated for comparison. (b) Experimental average mixing velocity $\tilde{U}$ measured in the convective regime as a function of the local adverse density difference $\Delta\tilde{\rho}'_m$. Each data point corresponds to the mean value $\pm$ standard deviation obtained from six independent repetitions of the same experimental condition. The dashed line shows the linear relation $\tilde{U} = 1.54 \times 10^{-5}\,\Delta\tilde{\rho}'_m$. (c) Dependence of the experimental onset time $\tilde{\tau}_D$ on $\Delta\tilde{\rho}'_m$. The dashed line corresponds to the regression $\log_{10}(\tilde{\tau}_D) = -1.46\,\log_{10}(\Delta\tilde{\rho}'_m) + 2.64$. The arrow indicates the experimental case used to compute the base-state density profile shown in panel (a). Details of the statistical analysis of the fitted parameters are provided in the text. All data points share the same color code and symbols as in Fig. 3(c) and Table III.

relation $\log_{10}(\tilde{\tau}_D) = a\,\log_{10}(\Delta\tilde{\rho}_m) + b$, with fitted parameters $a = -0.61$ (95% CI : $[-0.73, -0.49]$) and $b = 1.62$ (95% CI: [1.53, 1.70]), and $\mathsf{R}^2 = 0.9631$. The monotonic decrease of $\tilde{\tau}_D$ with $\Delta\tilde{\rho}_m$ confirms that the initiation of convection is governed by the adverse density jump generated by differential diffusion, in agreement with previous theoretical and numerical findings [33].

B. Pure DLC regime ($R \gg 1$, $\delta < 1$)

In the pure DLC regime, $\delta < 1$ such that the faster solute A is initially located in the upper, less dense layer and diffuses downward more rapidly than the lower solute B diffuses upward. Differential diffusion therefore produces a non-monotonic density profile in the vicinity of the initial contact line with a depletion zone above the position of the initial contact line and an accumulation zone below [see Fig. 5(a)] [17,22,33]. This generates two locally adverse density stratifications where $\partial\rho/\partial y < 0$, one in each layer [32]. These unstable regions drive locally the formation of two disconnected zones of convective rolls (see Fig. 2), while the overall stratification remains globally stable.

The experimental parameters corresponding to the pure DLC regimes studied here are summarized in Table III. As a representative example, we consider the case $(R, \delta) = (1.0354, 0.27)$ (Expt. 7), whose associated dimensionless base-state density profile is shown in Fig. 5(a). In contrast to the DD regime, the instability here is not governed by the global density difference $\Delta\rho_m$, but by the individual adverse density jump that develops within each layer, denoted $\Delta\rho'_m$. This quantity represents the local density difference across the unstable region where $\partial\rho/\partial y < 0$ and is equal, in the lower layer, to the density difference between the maximum in density and the density of the lower bulk of B. In the upper layer, it is the same difference in density measured then between the bulk density of A and the minimum. It therefore constitutes the effective driving force for the instability [33].

TABLE III. Combination of solutes used in the DLC regime. Each symbol correspond to the experiments shown in Figs. 3(c), 5(b), and 5(c). For each case, the experimentally measured dimensional solution densities, initial concentrations, diffusion ratio δ, buoyancy ratio R, dimensional initial density jump $\Delta\tilde{\rho}_0$, and dimensional dynamic density jumps $\Delta\tilde{\rho}_m$ and $\Delta\tilde{\rho}'_m$, are listed. In all cases, $\tilde{\rho}_0 = 998.0$ kg/m^3.

Expt.	Sym.	A	B	A_0 (M)	B_0 (M)	$\tilde{\rho}_A$ (kg/m^3)	$\tilde{\rho}_B$ (kg/m^3)	R	δ	$\Delta\tilde{\rho}_0$ (kg/m^3)	$\Delta\tilde{\rho}_m$ (kg/m^3)	$\Delta\tilde{\rho}'_m$ (kg/m^3)
1	●	NaCl	Suc.	1.00	0.40	1038.6	1050.6	1.2808	0.34	−12.0	−19.9651	3.9825
2	●	NaCl	Suc.	1.10	0.40	1042.6	1050.6	1.1659	0.34	−8.0	−17.4958	4.7479
3	●	NaCl	Suc.	1.20	0.40	1045.8	1050.6	1.0879	0.34	−4.8	−15.6113	5.4056
4	♦	KCl	Suc.	0.80	0.40	1035.1	1050.6	1.4178	0.27	−15.5	−24.8115	4.6558
5	♦	KCl	Suc.	0.90	0.40	1040.0	1050.6	1.2524	0.27	−10.6	−21.8933	5.6467
6	♦	KCl	Suc.	1.00	0.40	1044.3	1050.6	1.1361	0.27	−6.3	−19.4573	6.5786
7	♦	KCl	Suc.	1.10	0.40	1048.8	1050.6	1.0354	0.27	−1.8	−17.0290	7.6145
8	★	NaCl	Gly.	0.70	1.20	1026.3	1030.0	1.1201	0.66	−3.4	−5.5079	1.0540
9	▲	KCl	Gly.	0.60	1.20	1025.6	1030.0	1.1594	0.53	−4.4	−7.7348	1.6674

In practice, this dynamic density jump $\Delta\rho'_m$ is computed as

$$\Delta\rho'_m = \frac{\Delta\rho_m - \Delta\rho_0}{2} \quad \text{for } |\Delta\rho_0| < |\Delta\rho_m|, \tag{4}$$

and can be rescaled into dimensional units as $\Delta\tilde{\rho}'_m = \Delta\rho'_m(\tilde{\rho}_A - \tilde{\rho}_0)$.

The dependence of the mixing velocity $\tilde{U}$ on the local adverse density difference $\Delta\tilde{\rho}'_m$ is shown in Fig. 5(b). As in the pure DD regime, the experimental data exhibit a clear linear trend, which is well described by the weighted scaling $\tilde{U} = a \times 10^{-5}\,\Delta\tilde{\rho}'_m$, with a fitted coefficient $a = 1.54 \times 10^{-5}$ (95% CI: $[1.30 \times 10^{-5}, 1.79 \times 10^{-5}]$) and $\mathsf{R}^2_0 = 0.9112$. In contrast to the DD case, the fitted slope is smaller, reflecting the different driving mechanism in the DLC regime. Previous theoretical and numerical studies have shown that, for pure DLC, the proportionality constant relating $\tilde{U}$ to the adverse density difference is approximately half of that obtained in the DD regime [33]. The value measured here, 1.54×10^{-5}, is not only of the same order of magnitude as the theoretical prediction but also approximately half of the slope obtained for the DD case (3.60×10^{-5}), in quantitative agreement with the expected scaling.

The dependence of the onset time $\tilde{\tau}_D$ on the local adverse density difference $\Delta\tilde{\rho}'_m$ is presented in Fig. 5(c). As in the DD regime, the instability develops earlier when the driving density jump increases. All experimental data follow a clear weighted power-law trend $\log_{10}(\tilde{\tau}_D) = a\,\log_{10}(\Delta\tilde{\rho}'_m) + b$, with fitted parameters $a = -1.46$ (95% CI: $[-1.51, -1.41]$) and $b = 2.64$ (95% CI: [2.61, 2.67]), and $\mathsf{R}^2 = 0.9987$. Compared to the DD case, the slope in logarithmic scale is significantly larger in magnitude, indicating a stronger sensitivity of the onset time to variations in the adverse density difference. This steeper decay is consistent with previous studies of mixed RT-DD instabilities, where similar exponents were reported for the dependence of the onset time on the dynamic density jump for similar cell gaps [18].

IV. CONCLUSIONS

Differential diffusion can destabilize stratifications of a less dense solution above a denser one. We have here experimentally confirmed, in stratified Hele-Shaw systems, that the mixing properties of such buoyancy-driven instabilities are intrinsically governed by the adverse density jump dynamically generated by differential diffusion effects. These mechanisms, previously analyzed through theoretical and numerical studies, are here validated quantitatively experimentally.

For the pure DD instability, we have shown that the mixing velocity increases linearly with the dynamically generated density jump $\Delta\tilde{\rho}_m$, while the onset time $\tilde{\tau}_D$ decreases inversely

proportionally to it. These results confirm that the instability dynamics is controlled by the nonmonotonic density profile induced by differential diffusion rather than by the initial density jump. In the pure DLC regime, we have shown that the mixing dynamics are not determined by the global density difference either, but rather by the local adverse density jump between the density extremum and the adjacent bulk, denoted as $\Delta\tilde{\rho}'_m$, that develops independently within each unstable layer. Both the mixing velocity and the onset time scale with this locally induced density jump, highlighting the fundamentally local nature of the driving mechanism in this DLC regime. In both cases, the experimentally obtained relationships are consistent with the theoretically predicted scalings between the mixing velocity, the onset time, and the relevant dynamically generated adverse density jumps. The statistical analysis, including weighted regressions and confidence intervals for the fitted parameters, confirms that the observed trends are robust despite the inherent experimental variability associated with buoyancy-driven mixing experiments.

As the scalings we confirm experimentally can be deduced from a simple analytical computation of the dynamic density jump given by Eq. (3), this paves the way to an easy control of mixing properties of two-solute stratifications by a simple choice of δ via the selection of appropriate couples of solutes A and B and by tuning R via changes in concentrations.

These results provide a quantitative experimental validation of the theoretical framework previously developed for DD and DLC instabilities, paving the way for investigating more complex buoyancy-driven scenarios, including mixed instability modes [17,18,33]. Moreover, the present results are not restricted to Darcy-type flows in Hele-Shaw geometries, but may also guide future studies of stratified systems governed by the Navier-Stokes equations [34]. Future perspectives include analysis of similar mixing scalings in presence of nonideal diffusion [36,38], cross-diffusion [52–55], reactions [7,13,14,37,38,56], or flows [39] where differential diffusion effects can similarly generate dynamically induced density differences.

ACKNOWLEDGMENTS

D.M.E. and A.D. acknowledge the financial support of Prodex (Belgium) under Grant No. 4000144733. I.C. and A.D. acknowledge the CoPerMix project funded by the European Union's Horizon 2020 Research and Innovation Program under the Marie Sklodowska-Curie Grant Agreement No. 956457.

DATA AVAILABILITY

The data that support the findings of this article are not publicly available upon publication because it is not technically feasible and/or the cost of preparing, depositing, and hosting the data

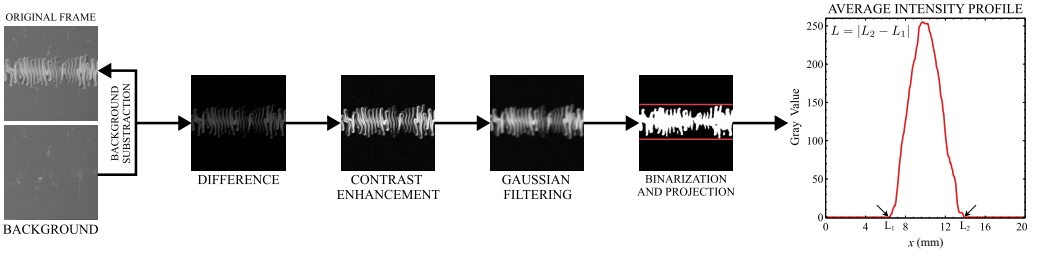

FIG. 6. Protocol used to compute L from the experimental images. A difference map was obtained by subtracting the background from each recorded frame. After contrast enhancement, a Gaussian filter was applied to reduce background noise, followed by a thresholding operation to generate a binary sequence. The mixing length L was determined from the y-averaged intensity profile as the distance between the first and last nonzero values of the profile.

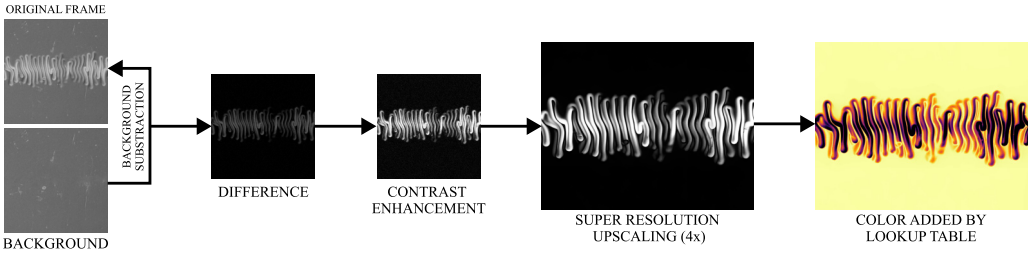

FIG. 7. Procedure used to rescale the experimental images shown in Fig. 2. The first three steps are identical to those described in Fig. 6. After contrast enhancement, the image sequence was processed using the Real-ESRGAN algorithm and upscaled up to four times relative to its original resolution. The resulting images were colored using the inverted `mpl_inferno` lookup table (LUT) available in FIJI.

would be prohibitive within the terms of this research project. The data are available from the authors upon reasonable request.

APPENDIX: METHODS USED TO COMPUTE THE MIXING LENGTH L AND TO IMPROVE THE QUALITY OF THE EXPERIMENTAL IMAGES

The mixing length L was computed from the experimental images at their original resolution. The image-processing protocol is summarized in Fig. 6. All processing steps were performed using ImageJ (FIJI) [57].

The snapshots presented in Fig. 2 are rescaled versions of the original experimental images obtained using the Real-ESRGAN method [58]. This rescaling was performed exclusively to enhance visual quality and does not affect the quantitative analysis. The procedure is illustrated in Fig. 7 and was also used to generate the videos included in the Supplemental Material [49].

[1] J. S. Turner, *Buoyancy Effects in Fluids* (Cambridge University Press, Cambridge, 1979).
[2] T. Menand and A. W. Woods, Dispersion, scale, and time dependence of mixing zones under gravitationally stable and unstable displacements in porous media, Water Resour. Res. **41**, 2004WR003701 (2005).
[3] M. S. D. Wykes and S. B. Dalziel, Efficient mixing in stratified flows: Experimental study of a Rayleigh–Taylor unstable interface within an otherwise stable stratification, J. Fluid Mech. **756**, 1027 (2014).
[4] D. R. Scott and D. J. Stevenson, Magma ascent by porous flow, J. Geophys. Res. **91**, 9283 (1986).
[5] R. W. Schmitt, Double diffusion in oceanography, Annu. Rev. Fluid Mech. **26**, 255 (1994).
[6] C. Almarcha, Y. R'Honi, Y. De Decker, P. M. J. Trevelyan, K. Eckert, and A. De Wit, Convective mixing induced by acid–base reactions, J. Phys. Chem. B **115**, 9739 (2011).
[7] L. Lemaigre, M. A. Budroni, L. A. Riolfo, P. Grosfils, and A. De Wit, Asymmetric Rayleigh-Taylor and double-diffusive fingers in reactive systems, Phys. Fluids **25**, 014103 (2013).
[8] D. M. Escala, M. A. Budroni, J. Carballido-Landeira, A. De Wit, and A. P. Muñuzuri, Self-organized traveling chemo-hydrodynamic fingers triggered by a chemical oscillator, J. Phys. Chem. Lett. **5**, 413 (2014).
[9] D. M. Escala and A. P. Munuzuri, Interface fingering instability triggered by a density-coupled oscillatory chemical reaction via precipitation, Langmuir **35**, 13769 (2019).
[10] A. De Wit, Chemo-hydrodynamic patterns and instabilities, Annu. Rev. Fluid Mech. **52**, 531 (2020).
[11] M. A. Budroni, L. Lemaigre, D. M. Escala, and A. De Wit, Buoyancy-driven chemohydrodynamic patterns in A + B → oscillator two-layer stratifications, Langmuir **39**, 997 (2023).

[12] H. E. Huppert and J. A. Neufeld, The fluid mechanics of carbon dioxide sequestration, Annu. Rev. Fluid Mech. **46**, 255 (2014).
[13] V. Loodts, H. Saghou, B. Knaepen, L. Rongy, and A. De Wit, Differential diffusivity effects in reactive convective dissolution, Fluids **3**, 83 (2018).
[14] M. Jotkar, L. Rongy, and A. De Wit, Reactive convective dissolution with differential diffusivities: Nonlinear simulations of onset times and asymptotic fluxes, Phys. Rev. Fluids **5**, 104502 (2020).
[15] T. Lei and K. H. Luo, Differential diffusion effects on density-driven instability of reactive flows in porous media, Phys. Rev. Fluids **5**, 033903 (2020).
[16] S. M. J. Raad, H. Hassanzadeh, and J. Ennis-King, On the dynamics of two-component convective dissolution in porous media, Water Resour. Res. **55**, 4030 (2019).
[17] J. Carballido-Landeira, P. M. J. Trevelyan, C. Almarcha, and A. De Wit, Mixed-mode instability of a miscible interface due to coupling between Rayleigh-Taylor and double-diffusive convective modes, Phys. Fluids **25**, 024107 (2013).
[18] S. S. Gopalakrishnan, J. Carballido-Landeira, B. Knaepen, and A. De Wit, Control of Rayleigh-Taylor instability onset time and convective velocity by differential diffusion effects, Phys. Rev. E **98**, 011101(R) (2018).
[19] J. S. Turner, Double-diffusive phenomena, Annu. Rev. Fluid Mech. **6**, 37 (1974).
[20] H. E. Huppert and J. S. Turner, Double-diffusive convection, J. Fluid Mech. **106**, 299 (1981).
[21] A. P. Stamp, G. O. Hughes, R. I. Nokes, and R. W. Griffiths, The coupling of waves and convection, J. Fluid Mech. **372**, 231 (1998).
[22] P. M. J. Trevelyan, C. Almarcha, and A. De Wit, Buoyancy-driven instabilities of miscible two-layer stratifications in porous media and Hele-Shaw cells, J. Fluid Mech. **670**, 38 (2011).
[23] T. Radko, *Double-Diffusive Convection* (Cambridge University Press, Cambridge, 2013).
[24] M. E. Stern and J. S. Turner, Salt fingers and convecting layers, Deep-Sea Res. Oceanogr. Abstr. **16**, 497 (1969).
[25] H. E. Huppert and R. S. J. Sparks, Double-diffusive convection due to crystallization in magmas, Annu. Rev. Earth Planet. Sci. **12**, 11 (1984).
[26] T. Green, Scales for double-diffusive fingering in porous media, Water Resour. Res. **20**, 1225 (1984).
[27] C. A. Cooper, R. J. Glass, and S. W. Tyler, Experimental investigation of the stability boundary for double-diffusive finger convection in a Hele-Shaw cell, Water Resour. Res. **33**, 517 (1997).
[28] S. E. Pringle and R. J. Glass, Double-diffusive finger convection: Influence of concentration at fixed buoyancy ratio, J. Fluid Mech. **462**, 161 (2002).
[29] R. W. Schmitt, J. R. Ledwell, E. T. Montgomery, K. L. Polzin, and J. M. Toole, Enhanced diapycnal mixing by salt fingers in the thermocline of the tropical Atlantic, Science **308**, 685 (2005).
[30] J. S. Turner and H. Stommel, A new case of convection in the presence of combined vertical salinity and temperature gradients, Proc. Natl. Acad. Sci. USA **52**, 49 (1964).
[31] R. W. Griffiths, Layered double-diffusive convection in porous media, J. Fluid Mech. **102**, 221 (1981).
[32] S. S. Gopalakrishnan, On the instability of buoyancy-driven flows in porous media, J. Fluid Mech. **892**, A13 (2020).
[33] S. S. Gopalakrishnan, B. Knaepen, and A. De Wit, Scalings of the mixing velocity for buoyancy-driven instabilities in porous media, J. Fluid Mech. **914**, A27 (2021).
[34] J. O. Oyero and A. De Wit, Scalings of mixing by buoyancy-driven instabilities in bulk flows: Effect of differential diffusion, Phys. Rev. Fluids **11**, 013503 (2026).
[35] Y. Luo and Y. Gong, Comparative study of buoyancy-driven instability for thermohaline stratification in a Hele-Shaw cell and extended geometry, Eng. Appl. Comput. Fluid Mech. **9**, 469 (2015).
[36] D. A. Bratsun, V. O. Oschepkov, E. A. Mosheva, and R. R. Siraev, The effect of concentration-dependent diffusion on double-diffusive instability, Phys. Fluids **34**, 034112 (2022).
[37] A. Mizev, E. Mosheva, and D. A. Bratsun, Extended classification of the buoyancy-driven flows induced by a neutralization reaction in miscible fluids. Part 1. Experimental study, J. Fluid Mech. **916**, A22 (2021).
[38] E. Mosheva, R. Siraev, and D. A. Bratsun, Control of chemoconvection in a rectangular slot by changing its spatial orientation, Fluids **8**, 98 (2023).

[39] E. Mosheva and I. Krasnyakov, Diffusive–layered convection in Y-shaped continuous-flow microreactor, Exp. Therm Fluid Sci. **151**, 111100 (2024).
[40] J. Martin, N. Rakotomalala, and D. Salin, Gravitational instability of miscible fluids in a Hele-Shaw cell, Phys. Fluids **14**, 902 (2002).
[41] E. Guyon, J. P. Hulin, L. Petit, and C. D. Mitescu, *Physical Hydrodynamics* (Oxford University Press, Oxford, 2015).
[42] Y. Shi and K. Eckert, A novel Hele-Shaw cell design for the analysis of hydrodynamic instabilities in liquid–liquid systems, Chem. Eng. Sci. **63**, 3560 (2008).
[43] *CRC Handbook of Chemistry and Physics: A Ready-Reference Book of Chemical and Physical Data*, 97th ed., edited by W. M. Haynes (CRC Press, Boca Raton, FL, 2017).
[44] C. Almarcha, P. M. J. Trevelyan, L. A. Riolfo, A. Zalts, C. El Hasi, A. D'Onofrio, and A. De Wit, Active role of a color indicator in buoyancy-driven instabilities of chemical fronts, J. Phys. Chem. Lett. **1**, 752 (2010).
[45] S. Kuster, L. A. Riolfo, A. Zalts, C. El Hasi, C. Almarcha, P. M. J. Trevelyan, A. De Wit, and A. D'Onofrio, Differential diffusion effects on buoyancy-driven instabilities of acid–base fronts: The case of a color indicator, Phys. Chem. Chem. Phys. **13**, 17295 (2011).
[46] G. S. Settles, *Schlieren and Shadowgraph Techniques: Visualizing Phenomena in Transparent Media*, Experimental Fluid Mechanics (Springer, Berlin, 2001).
[47] A. C. Ribeiro, O. Ortona, S. M. Simoes, C. I. Santos, P. M. Prazeres, A. J. Valente, V. M. Lobo, and H. D. Burrows, Binary mutual diffusion coefficients of aqueous solutions of sucrose, lactose, glucose, and fructose in the temperature range from (298.15 to 328.15) K, J. Chem. Eng. Data **51**, 1836 (2006).
[48] G. D'Errico, O. Ortona, F. Capuano, and V. Vitagliano, Diffusion coefficients for the binary system glycerol + water at 25 °C. A velocity correlation study, J. Chem. Eng. Data **49**, 1665 (2004).
[49] See Supplemental Material at http://link.aps.org/supplemental/10.1103/2d3q-f432 to visualize the movie files corresponding to cases $(R, \delta) = (1.1469,\ 1.51)$ for DD and $(R, \delta) = (1.0354,\ 0.27)$ for DLC.
[50] J. Kestin, H. E. Khalifa, and R. J. Correia, Tables of the dynamic and kinematic viscosity of aqueous NaCl solutions in the temperature range 20–150 °C and the pressure range 0.1–35 MPa, J. Phys. Chem. Ref. Data **10**, 71 (1981).
[51] N. S. Cheng, Formula for the viscosity of a glycerol-water mixture, Ind. Eng. Chem. Res. **47**, 3285 (2008).
[52] M. A. Budroni, L. Lemaigre, A. De Wit, and F. Rossi, Cross-diffusion-induced convective patterns in microemulsion systems, Phys. Chem. Chem. Phys. **17**, 1593 (2015).
[53] M. A. Budroni, Cross-diffusion-driven hydrodynamic instabilities in a double-layer system: General classification and nonlinear simulations, Phys. Rev. E **92**, 063007 (2015).
[54] M. C. Kim and K. H. Song, Theoretical and numerical analyses of the effect of cross-diffusion on the gravitational instability in ternary mixtures, Int. J. Heat Mass Transf. **143**, 118511 (2019).
[55] B. Šeta, J. Spangenberg, M. M. Bou-Ali, and V. Shevtsova, Impact of cross and main diffusion coefficients on symmetry breaking in nonreactive diffusion systems, Phys. Rev. E **112**, L033101 (2025).
[56] C. Almarcha, P. M. J. Trevelyan, P. Grosfils, and A. De Wit, Thermal effects on the diffusive layer convection instability of an exothermic acid-base reaction front, Phys. Rev. E **88**, 033009 (2013).
[57] J. Schindelin, I. Arganda-Carreras, E. Frise, V. Kaynig, M. Longair, T. Pietzsch, S. Preibisch, C. Rueden, S. Saalfeld, B. Schmid, *et al.*, Fiji: An open-source platform for biological-image analysis, Nat. Methods **9**, 676 (2012).
[58] X. Wang, L. Xie, C. Dong, and Y. Shan, Real-esrgan: Training real-world blind super-resolution with pure synthetic data, in *2021 IEEE/CVF International Conference on Computer Vision Workshops (ICCVW)* (IEEE, Piscataway, NJ, 2021), pp. 1905–1914.